Cell Reports

Report

Mpp6 Incorporation in the Nuclear Exosome Contributes to RNA Channeling through the Mtr4 Helicase

Graphical Abstract

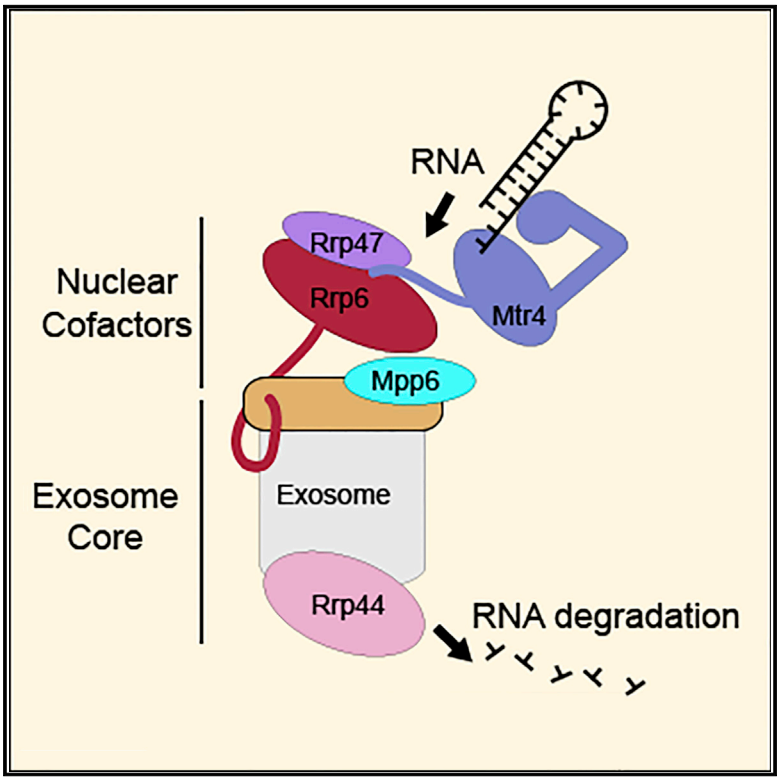

Authors

Sebastian Falk, Fabien Bonneau, Judith Ebert, Alexander Kögel, Elena Conti

Correspondence

conti@biochem.mpg.de

In Brief

Falk et al. provide insights into the structure and function of the nuclear RNA exosome. The authors elucidate how the nuclear cofactor Mpp6 is recruited to the exosome core complex and show that it facilitates the threading of RNA substrates from the Mtr4 helicase to the Rrp44 RNase.

Highlights

- Yeast Mpp6 is stably bound to the nuclear exosome core both in vivo and in vitro
- The Mpp6 middle domain binds the Rrp40 exosome subunit with conserved interactions
- Mpp6 enhances the ability of the Mtr4 helicase to channel RNA into the exosome core
- The pontocerebellar W238R mutation in human EXOSC3 affects the hMPP6-binding site

Accession Numbers

5OKZ

Falk et al., 2017, Cell Reports *20*, 2279–2286
September 5, 2017
http://dx.doi.org/10.1016/j.celrep.2017.08.033

CellPress

Cell Reports
Report

Mpp6 Incorporation in the Nuclear Exosome Contributes to RNA Channeling through the Mtr4 Helicase

Sebastian Falk,[1] Fabien Bonneau,[1] Judith Ebert,[1] Alexander Kögel,[1] and Elena Conti[1,2,*]
[1]Max-Planck-Institute of Biochemistry, Department of Structural Cell Biology, Am Klopferspitz 18, 82152 Martinsried/Munich, Germany
[2]Lead Contact
*Correspondence: conti@biochem.mpg.de
http://dx.doi.org/10.1016/j.celrep.2017.08.033

SUMMARY

The RNA-degrading exosome mediates the processing and decay of many cellular transcripts. In the yeast nucleus, the ubiquitous 10-subunit exosome core complex (Exo-9–Rrp44) functions with four conserved cofactors (Rrp6, Rrp47, Mtr4, and Mpp6). Biochemical and structural studies to date have shed insights into the mechanisms of the exosome core and its nuclear cofactors, with the exception of Mpp6. We report the 3.2-Å resolution crystal structure of a *S. cerevisiae* Exo-9–Mpp6 complex, revealing how linear motifs in the Mpp6 middle domain bind Rrp40 via evolutionary conserved residues. In particular, Mpp6 binds near a tryptophan residue of Rrp40 that is mutated in human patients suffering from pontocerebellar hypoplasia. Using biochemical assays, we show that Mpp6 is required for the ability of Mtr4 to extend the trajectory of an RNA entering the exosome core, suggesting that it promotes the channeling of substrates from the nuclear helicase to the processive RNase.

INTRODUCTION

The eukaryotic RNA exosome is a RNase complex that completely degrades or partially trims RNA substrates by successively cleaving their 3′ end nucleotides. The exosome is conserved from yeast to humans and acts on a wide variety of RNAs in turnover, surveillance, and processing pathways (Chlebowski et al., 2013; Kilchert et al., 2016). In the nucleus, the yeast exosome eliminates, for example, transcripts that are in excess or are defective, such as pre-mRNAs that failed to complete splicing and tRNAs that lack specific base modifications, and also destroys noncoding RNAs that are produced from leaky transcription initiation (reviewed in Chlebowski et al., 2013; Kilchert et al., 2016). Besides these destructive functions, the nuclear exosome is also involved in the maturation of rRNAs and small nuclear or small nucleolar RNAs (sn[o]RNAs) (Allmang et al., 1999). Defects in the nuclear functions of the exosome have been recently linked to a mutation in one of the exosome core subunits (yeast Rrp40/human EXOSC3) that is associated with a motor neuron degeneration disease (Fasken et al., 2017; Gillespie et al., 2017).

The processive core of the RNA exosome is a 10-protein complex (Exo-10) containing a single RNase subunit (Rrp44) and a catalytically inactive barrel (Exo-9), formed by six RNase PH-like proteins and three S1-KH "cap" proteins (reviewed in Zinder and Lima, 2017). Using biochemical and structural studies on the *S. cerevisiae* complex, we have previously shown that an RNA substrate is channeled from the entry pore at the top of Exo-9 to the Rrp44 exoribonuclease site via an internal conduit that is spanned by about 30 nucleotides (Bonneau et al., 2009; Makino et al., 2013a). The 30-nucleotide footprint of Exo-10 in vitro is reminiscent of a pre-rRNA processing defect common to yeast strains lacking functional nuclear exosome cofactors, namely the accumulation of a 5.8S rRNA precursor with a 3′ extension of 30 nucleotides (reviewed in Butler and Mitchell, 2011).

Studies over the last two decades have converged on four conserved nuclear exosome cofactors: Rrp6; Rrp47; Mtr4; and Mpp6 (reviewed in Butler and Mitchell, 2011; Kilchert et al., 2016). Rrp6 and its interacting partner Rrp47 are constitutively bound nuclear exosome subunits. Rrp6 contains a distributive 3′-5′ RNase domain that is positioned at the top of Exo-9 barrel (Makino et al., 2013a; Wasmuth et al., 2014; Zinder et al., 2016). Rrp47 does not have enzymatic activity but, together with Rrp6, forms a binding platform for recruiting Mtr4 (Schuch et al., 2014). Mtr4 is an essential helicase believed to assist the exosome by presenting it with suitably remodeled substrates that can be threaded with their unwound 3′ end into the degradation core (Johnson and Jackson, 2013; Makino et al., 2013b). In contrast to Rrp6, Rrp47, and Mtr4, there is currently no mechanistic structural information on Mpp6, a small basic protein lacking recognizable domains. Yeast Mpp6 is physically associated with the nuclear exosome in vivo (Milligan et al., 2008) and in vitro (Schuch et al., 2014) and is expected to bind near the cap protein Rrp40 (Shi et al., 2015). The precise role of Mpp6 in the nuclear functions of the exosome has remained elusive. In this work, we set out to shed light on the mechanisms with which yeast Mpp6 binds to and cooperates with the exosome.

RESULTS AND DISCUSSION

Yeast Mpp6 Binds the Exosome Core with High Affinity via the Middle Domain

We had previously shown that *S. cerevisiae* Mpp6 binds Exo-9 independently of Rrp6-Rrp47 and Rrp44 (Schuch et al., 2014).

To obtain a quantitative measure of the binding affinity, we introduced a single cysteine residue near the C terminus of full-length Mpp6 ($Mpp6^{FL}$ S184C substitution), labeled the purified protein with a cysteine-reactive fluorophore (red-maleimide) and performed microscale thermophoresis (MST) to analyze in the interaction with Exo-9. The MST measurements revealed that the Mpp6–Exo-9 dissociation constant is in the high nanomolar range (K_d ~82 nM; Figure 1A), indicating a relatively tight binding, albeit one order of magnitude weaker than that of Rrp6 (Kowalinski et al., 2016). Next, we compared endogenous nuclear exosomes purified from yeast strains genetically engineered to contain a Twin Strep-ProtA tag (TSPA) at the C terminus of either Mpp6 or Rrp6. In addition to tagging the nuclear cofactors, we also engineered strains with TSPA-tagged Ski7 (the cytoplasmic cofactor whose binding to Exo-9 is mutually exclusive with that of Rrp6; Kowalinski et al., 2016) and TSPA-tagged Rrp44 (the ubiquitous RNase that is present both in the nuclear and cytoplasmic exosome complexes). As expected, tandem-affinity purifications from the strain expressing Rrp44-TSPA yielded the exosome subunits, the cytoplasmic cofactor Ski7, and the nuclear cofactors Rrp6, Rrp47, and Mpp6 (Figure 1B, lane 5), whereas purifications from a strain expressing Ski7-TSAP precipitated the exosome core, but not the nuclear cofactors (Figure 1B, lane 6). In purifications from the Rrp6-TSPA-tagged strain, we detected the exosome subunits, Rrp47 and Mpp6 (Figure 1B, lane 7). Vice versa, purification using Mpp6-TSPA yielded the exosome, Rrp6 and Rrp47 (Figure 1B, lane 8). Thus, Mpp6 and Rrp6-Rrp47 can be part of the same endogenous exosome complexes. As a note, Mpp6 appears to be sub-stoichiometric with respect to other exosome components, either due to technical issues or its estimated lower abundance (Kulak et al., 2014). None of the purifications resulted in a significant co-precipitation of Mtr4 in the conditions we used (Figure 1B, lanes 5–8), suggesting that this is a transiently associated rather than a constitutively bound cofactor of the nuclear exosome.

Next, we mapped the domain of Mpp6 responsible for binding Exo-9. *S. cerevisiae* Mpp6 (186 residues) is an intrinsically disordered protein (Figures S1A and S1B). The N-terminal two-thirds of Mpp6 are evolutionary conserved, particularly at two hotspots between residues 11–21 and 111–115 (Milligan et al., 2008; Figures 1C and S1C). The C-terminal third is generally less conserved and contains a high percentage of positively charged residues. We purified several versions of glutathione S-transferase (GST)-tagged Mpp6 proteins and tested their interaction with untagged Exo-9 in pull-down assays with glutathione-agarose beads (Figure 1D). Removal of the C-terminal region of Mpp6 still allowed efficient binding to Exo-9 ($Mpp6^{1–122}$; Figure 1D, lane 9). However, a further C-terminal truncation (Mpp6 residues 1–110) impaired binding in the pull-down assay (Figure 1D, lane 10), suggesting the conserved 111- to 115-residue hotspot (Milligan et al., 2008) is involved in Exo-9 binding. Next, we truncated Mpp6 from the N terminus to progressively remove patches of conserved residues (Figures 1D, lanes 11–13, and S1C). We found that Mpp6 could be truncated to residues 83–122 and still interact with Exo-9 (Figure 1D, lane 12). However, a further truncation to residues 91–122 impaired binding (Figure 1D, compare lanes 12 and 13), suggesting that the 111- to 115-residue hotspot is not sufficient for Exo-9 binding. We concluded that the middle domain of Mpp6 (residues 83–122 or $Mpp6_M$) contains the major Exo-9-binding determinants (Figures 1C and S1C). We proceeded to obtain the three-dimensional structure of a minimal Exo-9–Mpp6 complex.

Overall Structure of Exo-9 Bound to Mpp6

Although we could obtain several crystal forms from Mpp6-containing exosome samples, upon solving these structures, we could only observe density for Exo-9. We reasoned that crystal-packing interactions might interfere with Mpp6 binding. From previous crosslinking and mass-spectrometry experiments, Mpp6 was expected to reside in close proximity to Rrp40 (Shi et al., 2015). Inspection of all crystal forms we had obtained indeed revealed that a surface of Rrp40 was involved in lattice interactions with an Rrp4 subunit from an adjacent complex in the crystal lattice (Figure S2A). To disrupt this contact without affecting Rrp40, we introduced mutations on the surface of Rrp4 involved in crystal packing (I66E, M68E, or Rrp4mut). The $Exo\text{-}9_{Rrp4mut}$–Mpp6 complex yielded diffracting crystals with four copies of the complex in the asymmetric unit (Figure S2B). Inspection of the map showed density for $Mpp6_M$ in two of the four copies. The final model was refined to 3.2 Å resolution with R_{free} of 26.2% and good stereochemistry (Table 1).

In the Mpp6-bound structure, Exo-9 has the typical barrel-like architecture that has been previously described for other exosome complexes, with a ring of six RNase PH-like proteins (Mtr3-Rrp42-Rrp41-Rrp45-Rrp46-Rrp43) capped by a ring of three S1/KH proteins (Rrp4, Rrp40, and Csl4; Kowalinski et al., 2016; Liu et al., 2006; Makino et al., 2013a, 2015; Wasmuth et al., 2014; Zinder et al., 2016). The most significant difference with previous X-ray structures is that the density for Csl4 is generally not well defined, in line with the increased flexibility of this subunit in the absence of Rrp6 (Makino et al., 2013a; Wang et al., 2007). $Mpp6_M$ binds on the surface of the Rrp40 subunit with two extended segments (Figure 2A).

The Mpp6 Middle Domain Wraps around Rrp40 with Evolutionary Conserved Interactions

Rrp40 contains three domains. The N-terminal domain is an all β-fold that binds on top of the Rrp46 subunit (Liu et al., 2006). The central S1 domain is a β-barrel characteristic of oligonucleotide/oligosaccharide-binding (OB)-fold proteins. The C-terminal domain is a type 1 KH domain, with a 3-stranded β-sheet packed against an α-helical bundle (Oddone et al., 2007). The KH β-sheet packs against the S1 domain, forming a single structural module that binds across the top of Rrp45, with the KH domain positioned on the outside of the ring and the S1 domain on the inside.

The longer segment of Mpp6 binds in a pocket formed between the S1 and KH domains of Rrp40 and could be unambiguously assigned to residues 108–117 (Figures 2B and S2C). This segment starts with van der Waal contacts of $Ile109_{Mpp6}$ with the first helix of the KH domain (at $Leu167_{Rrp40}$ and $Phe168_{Rrp40}$). It continues with a sharp 90° turn at $Gly111_{Mpp6}$ and ends with a β-strand that packs against and extends the β-sheet of the KH domain. The side chains of $Lys113_{Mpp6}$ and $Phe115_{Mpp6}$ protrude on one side of the β-strand toward the KH helical bundle and bind in a hydrophobic pocket lined by $Phe184_{Rrp40}$,

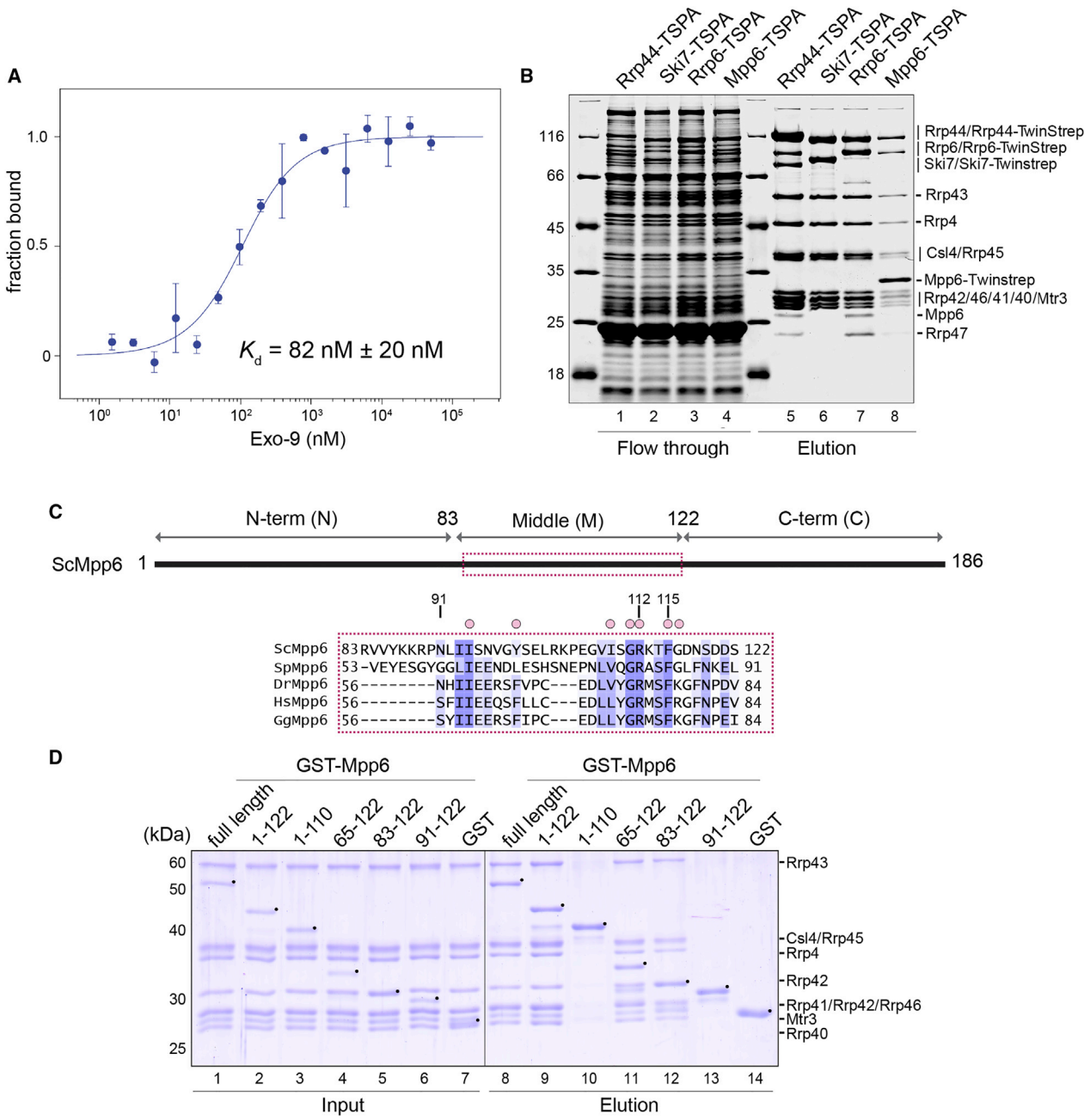

Figure 1. Mpp6 Binds with High Affinity to the Exo-9 Core via the Middle Domain

(A) The binding of Mpp6 to the Exo-9 core was measured with MST. The titration of Exo-9 ranged from 1.5 nM to 50 μM with a constant concentration of labeled Mpp6-S184C at 50 nM. Data were analyzed by thermophoresis and temperature jump mode. The error bars represent the SD of each data point calculated from three independent measurements.

(B) Tandem-affinity purification of exosome complexes using different bait proteins C-terminally tagged with a Twin Strep-ProtA tag (TSPA). Eluates were TCA precipitated and analyzed on 12% SDS-PAGE and stained with Instant Blue (Expedeon). Lanes 1–4 correspond to the flowthrough, and lanes 5–8 correspond to the elution.

(C) Schematic domain organization of yeast Mpp6, with the three domains (N-terminal, middle, and C-terminal) indicated. The conserved sequence motif of the middle domain is shown below the schematic representation (red box). The sequence alignment includes orthologs from the representative species. The level of conservation is indicated by color, from dark blue (high conservation) to white (no conservation). Above the sequence, residues of $Mpp6_M$ that interact with the Rrp40 are labeled with a salmon circle.

(D) Protein co-precipitations by GST pull-down assays. GST-tagged yeast $Mpp6^{FL}$ and truncations were purified and mixed with purified Exo-9. Pull-down assays were carried out using GSH-Sepharose beads in a buffer containing 100 mM NaCl. The Coomassie-stained 12% SDS-PAGE gels show the input (lanes 1–7) and the pulled-down protein precipitates (lanes 8–14). Black dots denote the bait protein.

Table 1. Crystallographic Data Collection and Refinement Statistics

Dataset	Exo-$9_{Rrp4mut}$–$Mpp6_M$
Space group	$P2_1$
Cell dimensions	
a, *b*, *c* (Å)	166.8, 237.4, 201.9
α, β, γ (°)	90.0, 110.4, 90.0
Data Collection	
Wavelength (Å)	1.25
Resolution (Å)	151.20–3.20
No. of reflections	996,533
No. of unique reflection	229,497
R_{merge} (%)	24.3 (229.9)
R_{pim} (%)	11.4 (129.8)
$I/\sigma I$	5.7 (0.6)
Completeness (%)	97.7 (79.9)
Multiplicity	4.3
$CC_{1/2}$	98.5 (24.3)
Refinement	
Resolution (Å)	80.76–3.20 (3.31–3.20)
No. of unique reflections	229,411
R_{work}/R_{free} (%)	22.5/26.2
Wilson B factor ($Å^2$)	72.27
Average B factors ($Å^2$)	95.3
No. of Atoms	
Proteins	66,857
Ligands	53
Stereochemistry	
Root-mean-square deviation (RMSD) bond lengths (Å)	0.003
RMSD bond angles (°)	0.52
Ramachandran favored (%)	96.0
Ramachandran outliers (%)	0.4

$Val186_{Rrp40}$, $Ile188_{Rrp40}$ and $Leu175_{Rrp40}$, $Ala179_{Rrp40}$. The side chain of $Arg112_{Mpp6}$ protrudes on the other side of the β- strand toward the S1 domain, engaging the aliphatic portion in apolar contacts with $Tyr120_{Rrp40}$ and $Leu150_{Rrp40}$ and engaging the guanidinium group in an electrostatic interaction with $Glu185_{Rrp40}$. Consistent with the structural analysis, mutation of $Arg112_{Mpp6}$ and $Phe115_{Mpp6}$ (R112E, F115A mutant) impaired the interaction of $Mpp6^{FL}$ with Exo-9 in pull-down assays with recombinant proteins (Figure 2C, compare lanes 3 and 4).

In the case of the shorter segment of Mpp6, the interpretation of the density was rather ambiguous. This segment extends on a conserved surface of the Rrp40 N-terminal domain (above the Leu21-Gly22-Pro23-Gly24 loop) and contacts the edge of the KH helical bundle (at Arg164, Phe168). Guided by the density features of Mpp6, sequence conservation, results of the mapping experiments (Figure 1D), and by chemical considerations, we tentatively assigned the sequence of the Mpp6 shorter segment to residues 90–99 (Figure S2D). The structural model is consistent with geometric restraints deduced from previous mass spectrometry-crosslinking data (e.g., a distance of less than 30 Å between crosslinked Mpp6 Lys104–Rrp40 Lys49 and between crosslinked Mpp6 Lys113–Rrp40 Lys176; Figure S2E; Shi et al., 2015).

The Human EXOSC3 W238R Disease Mutation Affects Binding of Mpp6

The evolutionary conservation of the *S. cerevisiae* Mpp6-Rrp40 interactions suggested that the human orthologs hMPP6-EXOSC3 engage in a similar binding mode. Mutations of human Rrp40 (EXOSC3) are associated with pontocerebellar hypoplasia, a severe and often deadly motor neuron disease in children (Wan et al., 2012). The most severe phenotypes are linked to the mutation of $Trp238_{EXOSC3}$ to arginine (Wan et al., 2012). Previous studies have shown that the corresponding mutation of yeast $Trp195_{Rrp40}$ to arginine (W195R) affects cell growth and impacts specifically on the nuclear functions rather than the cytoplasmic functions of the exosome (Fasken et al., 2017), particularly rRNA processing (Gillespie et al., 2017). From the Exo-9–Mpp6 structure, the yeast Rrp40 W195R mutation is predicted to cause an unfavorable and likely incompatible electrostatic environment for accommodating $Arg112_{Mpp6}$ (corresponding to human hMPP6 Arg74). We tested the effect of mutating hMPP6 and EXOSC3 in in vitro binding experiments with recombinant proteins. Whereas the middle domain of hMPP6 interacted with human EXO-9 in the pull-down assays, an hMPP6 mutant containing the R74E, F77A substitution failed to do so (Figure 2D), similarly to the results we had obtained with the corresponding yeast Mpp6 R112E, F115A mutant (Figure 2C). Next, we reconstituted a human hEXO-9 complex containing the W238R disease mutation. Under low ionic strength conditions (100 mM NaCl), the interaction between hMPP6 and hEXO-9 mutant was weakened (Figure 2E, compare lanes 3 and 5). Applying more stringent washing conditions (e.g., increasing the ionic strength to 500 mM NaCl) strongly reduced the binding of hMPP6 to the hEXO-9 mutant (Figure 2E, compare lanes 4 and 6). This suggests that the EXOSC3 W238R mutant destabilizes the hMPP6-binding surface of EXOSC3, providing a mechanistic explanation for the impact of this mutation on the functions of the nuclear exosome. Whether hMPP6 recruitment is the ultimate deficit in pontocerebellar hypoplasia patients remains unclear, because in human cells, the hMPP6-binding surface could in principle be used to recruit another nuclear cofactor and destabilization of this surface might also lead to instability of the protein in vivo (Fasken et al., 2017).

The Presence of Mpp6 in the Nuclear Exosome Supports Efficient RNA Channeling through Mtr4

How does Mpp6 binding on top of the exosome core impact on the biochemical properties and functions of the nuclear exosome? Because Mpp6 has been shown to have RNA-binding properties (Milligan et al., 2008; Schilders et al., 2005), we analyzed its contribution to the nuclear exosome complex using RNase protection assays (Figures 3A and S3). Using these assays, we have previously shown that yeast Exo-10 has an RNA-binding footprint of about 30 nucleotides (Bonneau et al., 2009), reflecting the RNA-binding path in the internal channel of Exo-10 (Makino et al., 2013a). The presence of Rrp6-Rrp47

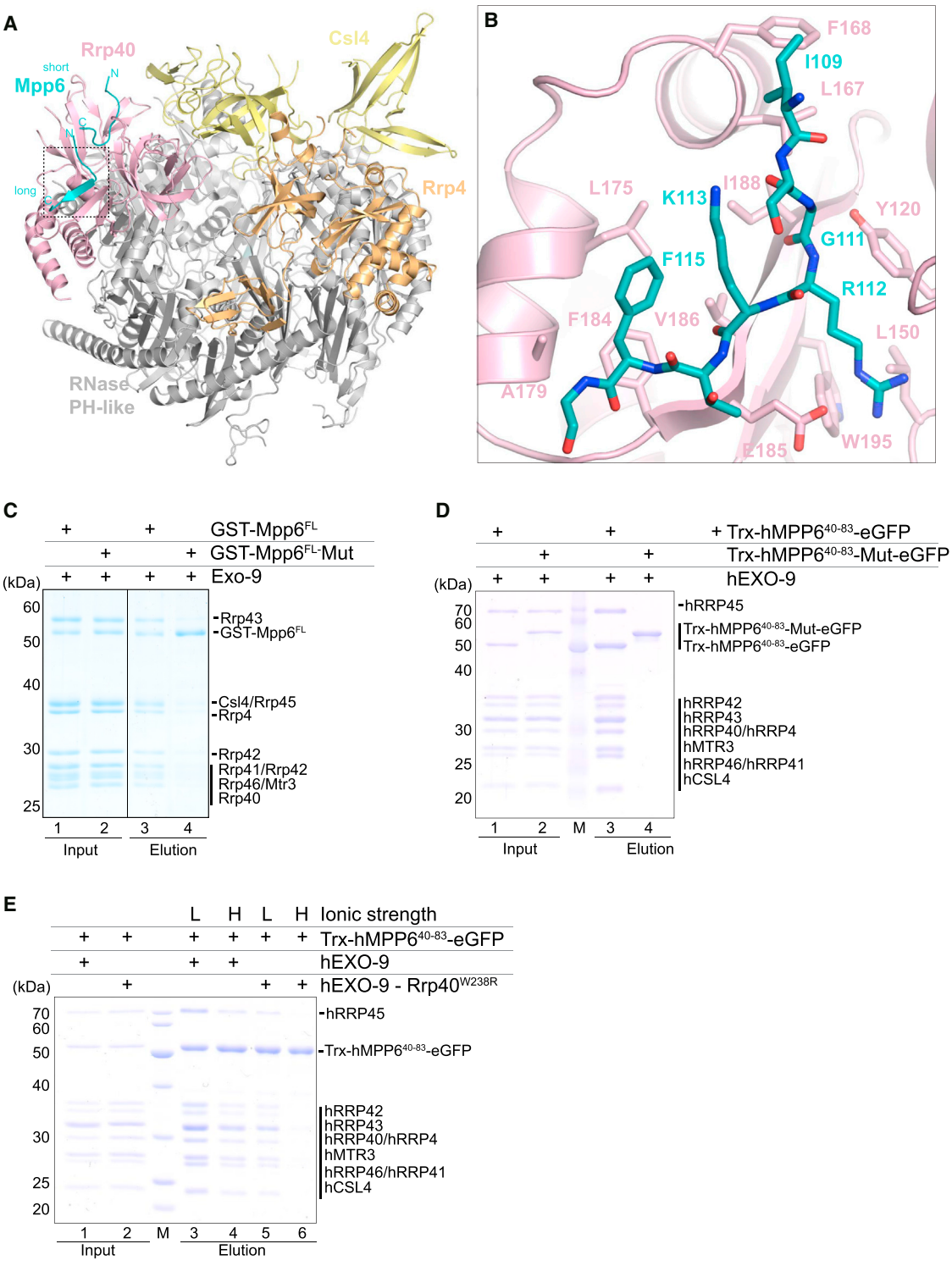

Figure 2. Crystal Structure of Mpp6 Middle Domain Bound to Exo-9 (to Rrp40)

(A) Crystal structure of the *S. cerevisiae* Exo-9–Mpp6 complex (shown in a "front" view). The RNase PH-like core is in gray and the cap proteins Csl4, Rrp4, and Rrp40 in yellow, orange, and salmon, respectively. Mpp6 is shown in cyan, and the N- and C-termini of Mpp6 are indicated.

(B) Zoom-in views of the Mpp6-Rrp40 interaction interface at the long region in the same colors as in (A). Conserved residues involved in the interaction are shown in stick representation.

(legend continued on next page)

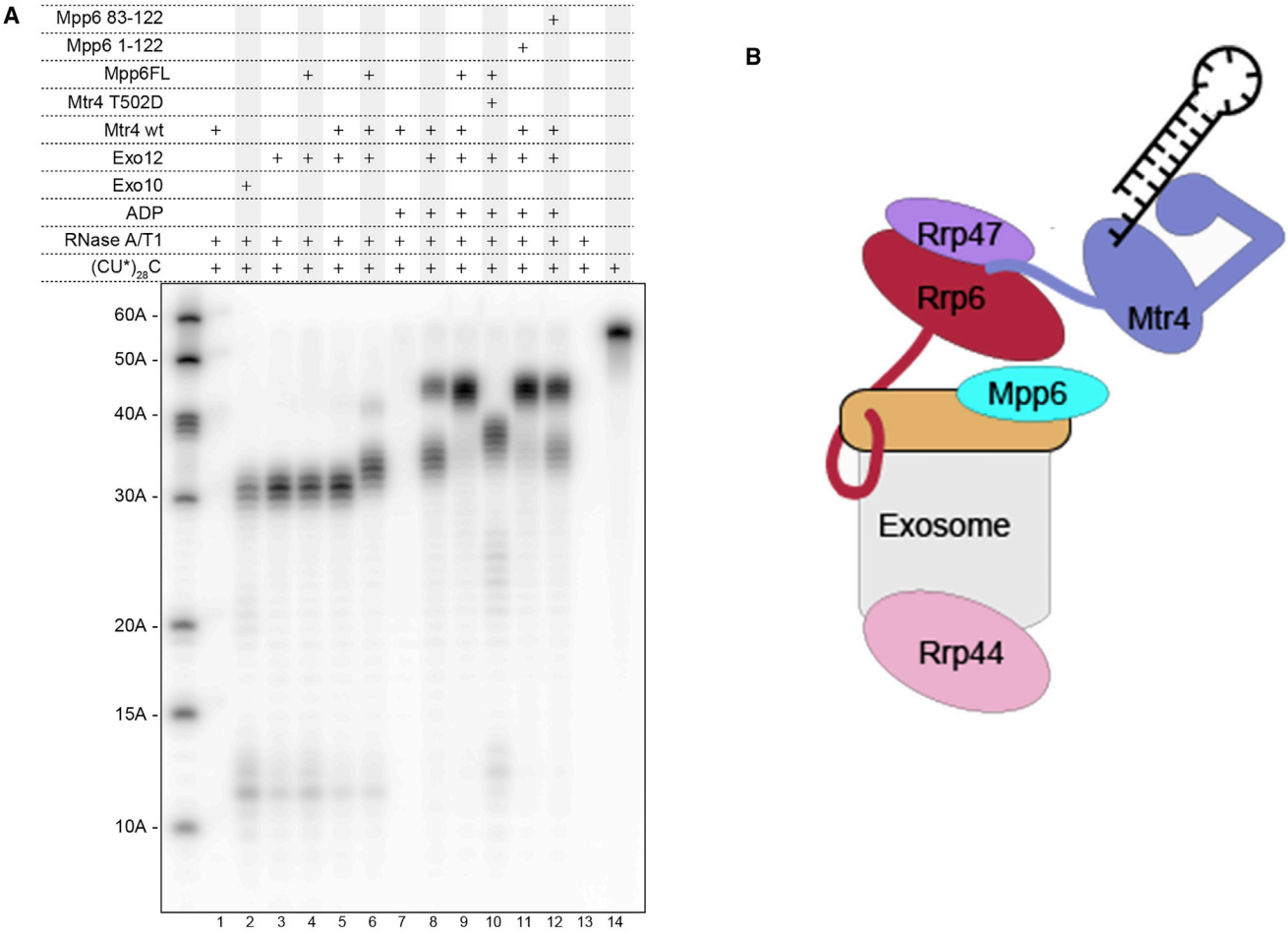

Figure 3. Mpp6 Supports Efficient RNA Channeling through the Mtr4–Exosome Complex

(A) RNase protection patterns of the nuclear exosome. A single-stranded $(C^*U)_{28}C$ RNA, internally ^{32}P-labeled at the uridine phosphate, was incubated with different combinations of components of the nuclear exosome as indicated and treated with RNase A/T1 (as in Bonneau et al., 2009). The reaction products were analyzed by denaturing PAGE and phosporimaging. RNA fragments of ~30-nt length accumulated in the presence of Exo-10 and Exo-12. Longer RNA fragments of ~45 nt accumulated in the presence of Exo-12 and Mtr4, ADP, and Mpp6.

(B) Model of Mtr4 recruitment and RNA targeting to the nuclear exosome complex. The model recapitulates structural features and interactions of nuclear exosome components from this work and from previous studies (Weir et al., 2010; Jackson et al., 2010; Makino et al., 2013a, 2015; Schuch et al., 2014; Wasmuth et al., 2014; Zinder et al., 2016).

on Exo-10 intensified but did not shift the size of the protected fragments (Figure 3A, lanes 2 and 3). This is consistent with the stabilizing effects of Rrp6 (Makino et al., 2013a) and with the features of the Exo-10–Rrp6–Rrp47 (Exo-12) structure (Makino et al., 2015). Addition of the Mtr4 helicase led to a partial shift to 45-nucleotide-long RNA fragments but only in the presence of ADP (compare lane 8 and lane 5). Further addition of Mpp6 completely shifted the protection pattern to the 45-nucleotide fragments in the presence of ADP (lane 9). Because Mtr4 is an ATP-dependent RNA helicase, we speculate that productive RNA binding and channeling depends on the presence of nucleotides.

These results suggested that, in the context of 14-subunit complex, Mpp6 helps recruiting or holding Mtr4 in a conformation

(C) Protein co-precipitations with GST-tagged yeast $Mpp6^{FL}$ and Mpp6 R112E/F115A (Mpp6-Mut). The pull-down assays were carried out as in Figure 1D. The Coomassie-stained 12% SDS-PAGE gels show the input (lanes 1 and 2) and the pulled-down protein precipitates (lanes 3 and 4).

(D) Protein co-precipitations with Trx-eGFP-tagged human MPP6 residues 40–83 (Trx-$hMPP6^{40–83}$-eGFP) and MPP6 R74E/F77A (Trx-$hMPP6^{40–83}$-Mut-eGFP). The pull-down assays were carried out using GFP-binder Sepharose beads in a buffer containing 100 mM NaCl. The Coomassie-stained 12% SDS-PAGE gels show the input (lanes 1 and 2) and the pulled-down protein precipitates (lanes 3 and 4).

(E) Protein co-precipitations with Trx-eGFP-tagged human MPP6 residues 40–83 (Trx-$hMPP6^{40–83}$-eGFP) and purified hEXO-9 (either wild-type or hExo-9-$Rrp40^{W238R}$). Pull-down assays were carried out using GFP-binder Sepharose beads in either 100 mM or 500 mM NaCl. The Coomassie-stained 12% SDS-PAGE gels show the input (lanes 1 and 2) and the pulled-down protein precipitates (lanes 3–6).

whereby the helicase channel can form a continuous conduit with the exosome core. To confirm the presence of an Mtr4-channel-dependent path to the exosome, we introduced an unfavorable negative charge by substituting a conserved RNA-binding residue in the helicase channel (Thr502Asp; Weir et al., 2010). The presence of the Mtr4 T502D mutant indeed impaired the 45-nucleotide pattern (lane 10), leading to an intermediate shift (whose significance is currently unclear). Interestingly, the C-terminal domain of Mpp6 could be removed without affecting the accumulation of the 45-nucleotide fragments ($Mpp6^{1–122}$; lane 11). However, the Exo-9-binding domain of Mpp6 ($Mpp6_M$; residues 83–122) was not as efficient as the fragment encompassing residues 1–122 in promoting the accumulation of the 45-nucleotide fragments, suggesting that the N-terminal domain contributes to hold Mtr4 in the RNA-channeling conformation on top of the exosome core, although the detailed mechanisms are currently unclear.

In summary, the emerging picture from our study is that Mpp6 stably binds Exo-12 to form a nuclear exosome population (Exo-13) that can effectively recruit the more transient fourteenth subunit, Mtr4 (Figure 3B). We speculate that, in an endogenous context, protein-protein interactions might not be sufficient to recruit Mtr4 and that the helicase might have to be productively engaged with an RNA substrate to be efficiently targeted to the nuclear exosome. Such targeting would in turn result in the channeling of the RNA substrate from the unwinding helicase to the processive RNase of the nuclear exosome complex.

EXPERIMENTAL PROCEDURES

See the Supplemental Information for detailed methods.

Recombinant Protein Expression and Purification

Exosome proteins and cofactors were expressed and purified as previously described (Falk et al., 2014; Greimann and Lima, 2008; Makino et al., 2013a). The yeast Exo-9–Mpp6 complex was reconstituted by mixing Exo-9 with 1.2-fold molar excess of Mpp6 full-length followed by gel filtration. Human MPP6 residues 40–83 were tagged with an N-terminal His_6-thioredoxin-tag (His-Trx) and a C-terminal eGFP-StrepII-tag.

Endogenous Protein Purification

All yeast strains generated here are derivatives of the base strain BY4741 (MATa his3Δ1 leu2Δ0 met15Δ0 ura3Δ0). General yeast manipulations were conducted by standard methods.

Biochemical Assays

Pull-down assays with GST-tagged *S. cerevisiae* Mpp6 were carried out with GSH Sepharose (GE Healthcare). Pull-down assays with GFP-tagged human MPP6 were carried out with GFP binder resin. The tagged bait proteins were incubated with 1.2 molar excess of untagged prey (Exo-9) and washed three times with a buffer containing either 100 mM or 500 mM NaCl. RNase protection was carried out as previously described (Bonneau et al., 2009).

Biophysical Assays

The microscale thermophoresis experiments were carried out with Mpp6 S184C labeled with red maleimide incubated with increasing concentrations of unlabeled Exo-9 in a buffer containing 150 mM NaCl. Thermophoresis was measured with an light-emitting diode (LED) power of 40% and standard parameters on a NanoTemper Monolith NT.115 machine. Titrations were performed in triplicates, and the data were analyzed using the Thermophoresis and T-Jump strategy option with the MO software (NanoTemper Technologies).

Crystallization and Structure Determination

The best diffracting crystals of the Exo-9–Mpp6 complex were obtained at 12 mg/mL in 0.1 M Tris/Mops (pH 7.5), 30 mM $MgCl_2$, 30 mM $CaCl_2$, and 30% polyethylengylcol (PEG) 8000/ethylene glycol. X-ray data were collected at 100 K at the beamline PXII (X10SA) of the Swiss Light Source (SLS) (Villigen, Switzerland). The structure was solved by molecular replacement of the coordinates of Exo-9 from PDB 5JEA (Kowalinski et al., 2016). Data processing, phasing, model building, and refinement were carried out with standard programs (as detailed in Supplemental Information).

ACCESSION NUMBERS

The accession number for the coordinates and structure factors for the Exo-9–Mpp6 complex reported in this paper is PDB: 5OKZ.

SUPPLEMENTAL INFORMATION

Supplemental Information includes Supplemental Experimental Procedures and three figures and can be found with this article online at http://dx.doi.org/10.1016/j.celrep.2017.08.033.

AUTHOR CONTRIBUTIONS

S.F. and E.C. initiated the project; J.E. obtained crystals; A.K. performed the work in Figures 2E and 2F; F.B. performed the work in Figures 2B and 3; S.F. carried out all other experiments in the paper; and S.F. and E.C. wrote the manuscript.

ACKNOWLEDGMENTS

We would like to thank Jérôme Basquin, Karina Valer-Saldaña, and Sabine Pleyer at the MPI-Martinsried crystallization facility and the staff of the PX beamlines of the SLS synchrotron for assistance in data collection. This study was supported by the Max Planck Gesellschaft, the European Research Council (ERC Advanced Investigator Grant 294371), and the Deutsche Forschungsgemeinschaft (SFB1035, GRK1721, and Cluster of Excellence CIPSM).

Received: June 20, 2017
Revised: July 27, 2017
Accepted: August 11, 2017
Published: September 5, 2017

REFERENCES

Allmang, C., Kufel, J., Chanfreau, G., Mitchell, P., Petfalski, E., and Tollervey, D. (1999). Functions of the exosome in rRNA, snoRNA and snRNA synthesis. EMBO J. *18*, 5399–5410.

Bonneau, F., Basquin, J., Ebert, J., Lorentzen, E., and Conti, E. (2009). The yeast exosome functions as a macromolecular cage to channel RNA substrates for degradation. Cell *139*, 547–559.

Butler, J.S., and Mitchell, P. (2011). Rrp6, rrp47 and cofactors of the nuclear exosome. Adv. Exp. Med. Biol. *702*, 91–104.

Chlebowski, A., Lubas, M., Jensen, T.H., and Dziembowski, A. (2013). RNA decay machines: the exosome. Biochim. Biophys. Acta *1829*, 552–560.

Falk, S., Weir, J.R., Hentschel, J., Reichelt, P., Bonneau, F., and Conti, E. (2014). The molecular architecture of the TRAMP complex reveals the organization and interplay of its two catalytic activities. Mol. Cell *55*, 856–867.

Fasken, M.B., Losh, J.S., Leung, S.W., Brutus, S., Avin, B., Vaught, J.C., Potter-Birriel, J., Craig, T., Conn, G.L., Mills-Lujan, K., et al. (2017). Insight into the RNA exosome complex through modeling pontocerebellar hypoplasia type 1b disease mutations in yeast. Genetics *205*, 221–237.

Gillespie, A., Gabunilas, J., Jen, J.C., and Chanfreau, G.F. (2017). Mutations of EXOSC3/Rrp40p associated with neurological diseases impact ribosomal RNA processing functions of the exosome in S. cerevisiae. RNA *23*, 466–472.

Greimann, J.C., and Lima, C.D. (2008). Reconstitution of RNA exosomes from human and Saccharomyces cerevisiae cloning, expression, purification, and activity assays. Methods Enzymol. *448*, 185–210.

Jackson, R.N., Klauer, A.A., Hintze, B.J., Robinson, H., van Hoof, A., and Johnson, S.J. (2010). The crystal structure of Mtr4 reveals a novel arch domain required for rRNA processing. EMBO J. *29*, 2205–2216.

Johnson, S.J., and Jackson, R.N. (2013). Ski2-like RNA helicase structures: common themes and complex assemblies. RNA Biol. *10*, 33–43.

Kilchert, C., Wittmann, S., and Vasiljeva, L. (2016). The regulation and functions of the nuclear RNA exosome complex. Nat. Rev. Mol. Cell Biol. *17*, 227–239.

Kowalinski, E., Kögel, A., Ebert, J., Reichelt, P., Stegmann, E., Habermann, B., and Conti, E. (2016). Structure of a cytoplasmic 11-subunit RNA exosome complex. Mol. Cell *63*, 125–134.

Kulak, N.A., Pichler, G., Paron, I., Nagaraj, N., and Mann, M. (2014). Minimal, encapsulated proteomic-sample processing applied to copy-number estimation in eukaryotic cells. Nat. Methods *11*, 319–324.

Liu, Q., Greimann, J.C., and Lima, C.D. (2006). Reconstitution, activities, and structure of the eukaryotic RNA exosome. Cell *127*, 1223–1237.

Makino, D.L., Baumgärtner, M., and Conti, E. (2013a). Crystal structure of an RNA-bound 11-subunit eukaryotic exosome complex. Nature *495*, 70–75.

Makino, D.L., Halbach, F., and Conti, E. (2013b). The RNA exosome and proteasome: common principles of degradation control. Nat. Rev. Mol. Cell Biol. *14*, 654–660.

Makino, D.L., Schuch, B., Stegmann, E., Baumgärtner, M., Basquin, C., and Conti, E. (2015). RNA degradation paths in a 12-subunit nuclear exosome complex. Nature *524*, 54–58.

Milligan, L., Decourty, L., Saveanu, C., Rappsilber, J., Ceulemans, H., Jacquier, A., and Tollervey, D. (2008). A yeast exosome cofactor, Mpp6, functions in RNA surveillance and in the degradation of noncoding RNA transcripts. Mol. Cell. Biol. *28*, 5446–5457.

Oddone, A., Lorentzen, E., Basquin, J., Gasch, A., Rybin, V., Conti, E., and Sattler, M. (2007). Structural and biochemical characterization of the yeast exosome component Rrp40. EMBO Rep. *8*, 63–69.

Schilders, G., Raijmakers, R., Raats, J.M., and Pruijn, G.J. (2005). MPP6 is an exosome-associated RNA-binding protein involved in 5.8S rRNA maturation. Nucleic Acids Res. *33*, 6795–6804.

Schuch, B., Feigenbutz, M., Makino, D.L., Falk, S., Basquin, C., Mitchell, P., and Conti, E. (2014). The exosome-binding factors Rrp6 and Rrp47 form a composite surface for recruiting the Mtr4 helicase. EMBO J. *33*, 2829–2846.

Shi, Y., Pellarin, R., Fridy, P.C., Fernandez-Martinez, J., Thompson, M.K., Li, Y., Wang, Q.J., Sali, A., Rout, M.P., and Chait, B.T. (2015). A strategy for dissecting the architectures of native macromolecular assemblies. Nat. Methods *12*, 1135–1138.

Wan, J., Yourshaw, M., Mamsa, H., Rudnik-Schöneborn, S., Menezes, M.P., Hong, J.E., Leong, D.W., Senderek, J., Salman, M.S., Chitayat, D., et al. (2012). Mutations in the RNA exosome component gene EXOSC3 cause pontocerebellar hypoplasia and spinal motor neuron degeneration. Nat. Genet. *44*, 704–708.

Wang, H.-W., Wang, J., Ding, F., Callahan, K., Bratkowski, M.A., Butler, J.S., Nogales, E., and Ke, A. (2007). Architecture of the yeast Rrp44 exosome complex suggests routes of RNA recruitment for 3′ end processing. Proc. Natl. Acad. Sci. USA *104*, 16844–16849.

Wasmuth, E.V., Januszyk, K., and Lima, C.D. (2014). Structure of an Rrp6-RNA exosome complex bound to poly(A) RNA. Nature *511*, 435–439.

Weir, J.R., Bonneau, F., Hentschel, J., and Conti, E. (2010). Structural analysis reveals the characteristic features of Mtr4, a DExH helicase involved in nuclear RNA processing and surveillance. Proc. Natl. Acad. Sci. USA *107*, 12139–12144.

Zinder, J.C., and Lima, C.D. (2017). Targeting RNA for processing or destruction by the eukaryotic RNA exosome and its cofactors. Genes Dev. *31*, 88–100.

Zinder, J.C., Wasmuth, E.V., and Lima, C.D. (2016). Nuclear RNA exosome at 3.1 Å reveals substrate specificities, RNA paths, and allosteric inhibition of Rrp44/Dis3. Mol. Cell *64*, 734–745.

Cell Reports, Volume *20*

Supplemental Information

Mpp6 Incorporation in the Nuclear Exosome Contributes to RNA Channeling through the Mtr4 Helicase

Sebastian Falk, Fabien Bonneau, Judith Ebert, Alexander Kögel, and Elena Conti

Figure S1

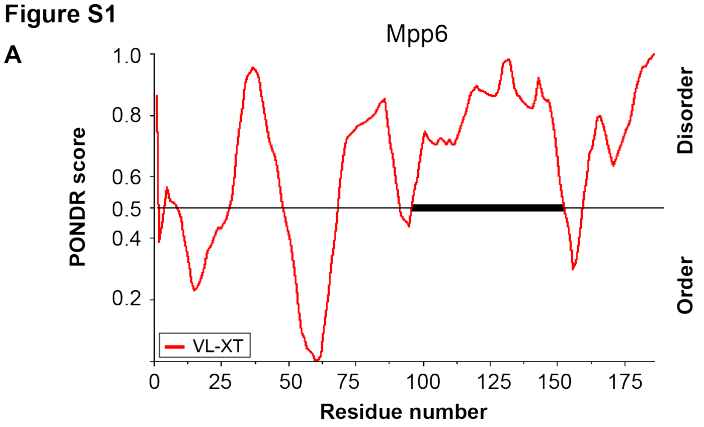

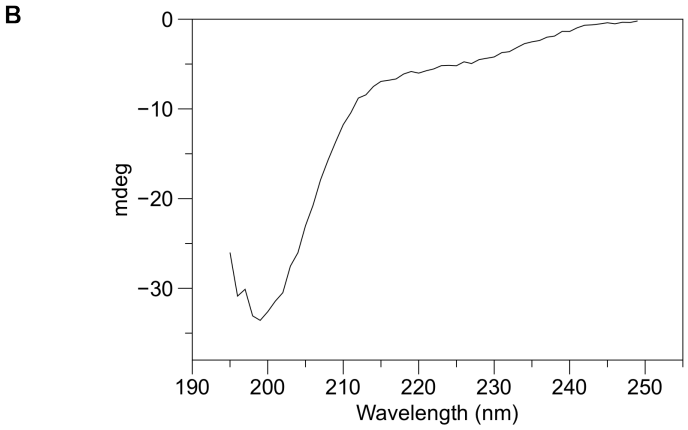

C

```
ScMpp6/1-186      1 MSANNGVTGKLSSRVMNMKFMKFGKTDDEESSNSNTPSNINSDVEPIEQKGKLFGLDDSAWDLNSYKDDLKKIS 74
SpMpp6/1-188      1 ----------MSSKLLSMKFMQRARGIDPKQAEEELSKNIVTDEH---------------WSLAGKVDFLPQKM 49
DrMpp6/1-168      1 M-ANDGGA-KLSKNLLRMKFMQRGLDAEVKKQLDEEEKRIISDEH---------------WFL-----DLPELK 52
HsMpp6/1-160      1 M-AAERKT-RLSKNLLRMKFMQRGLDSETKKQLEEEEKKIISEEH---------------WYL-----DLPELK 52
GgMpp6/1-164      1 M-AGEVKT-KLSKNLLRMKFMQRGLDSQTKKQLDEEEKKIISDEH---------------WYL-----DLPDLK 52

ScMpp6/1-186     75 GKEKKKVKRVVYKKRPNLIISNVGYSELRKPEGVISGRKTFGDNSDDSGSRKRKFDEGEQNED----------137
SpMpp6/1-188     50 TRN------VEYESGYGGLIEENDLESHSNEPNLVQGRASFGLFNKELGEENVDEKDVSKNEEVDVNG----TK113
DrMpp6/1-168     53 AKE------------NHIIEERSFVPC---EDLVYGRMSFKGFNPDVEKLMLLMNAPREEEDEEEEDESMNKM110
HsMpp6/1-160     53 EKE------------SFIIEEQSFLLC---EDLLYGRMSFRGFNPEVEKLMLQMNAKHKAEEVEDE-----TV105
GgMpp6/1-164     53 EKE------------SYIIEERSFIPC---EDLLYGRMSFKGFNPEIEKLMVQINSKSKKEEIEEDD----KM106

ScMpp6/1-186    138 -------EKRDAKDKEFTGSQDDG----------EDEYDLDKLFKDSIKKKKTNHNGKNKNRNSKK------186
SpMpp6/1-188    114 ITDTSELTERERRKQELVSKKAEASRKMEVKAPAKESKKRKVNELSQDVISLHSPKESNARKTKKNKNKKKKR187
DrMpp6/1-168    111 ETDITD-EEMAKRYQSLVES----------------MRKKFAKKRDRSAVSNKEDVNCNVTDDIRPKRAFMKPQ167
HsMpp6/1-160    106 ELDVSD-EEMARRYETLVGT----------------IGKKFARKRDH---ANYEEDENGDITPIKAKKMFLKPQ159
GgMpp6/1-164    107 EADVSD-EEMARRYETLVGT----------------IGKKFLKKRDQRVLHDEDEEENSNTKPKKARKMFLKPQ163
```

Figure S1, related to Figure 1. Mpp6 in an intrinsically disordered and conserved protein. (**A**) Sequence analysis predicts yeast Mpp6 as intrinsically disordered. Bioinformatic disorder prediction analysis of *S. cerevisiae* Mpp6 (1-186) with the program PONDR (Li et al., 1999). (**B**) Analysis of Mpp6 secondary structure using far-UV CD spectroscopy indicates that Mpp6 is unfolded in solution. The far-UV CD spectrum exhibits a pronounced minimum around 200 nm and only weak ellipticity above 210 nm, which is characteristic for unfolded proteins. (**C**) Sequence alignment of full-length Mpp6 with orthologues from the representative species *Saccharomyces cerevisiae* (Sc), *Schizosaccharomyces pombe* (Sp), *Homo sapiens* (Hs), *Danio rerio* (Dr) and *Gallus gallus* (Gg).The level of conservation is indicated by color: from dark blue (high conservation) to white (no conservation).

Figure S2

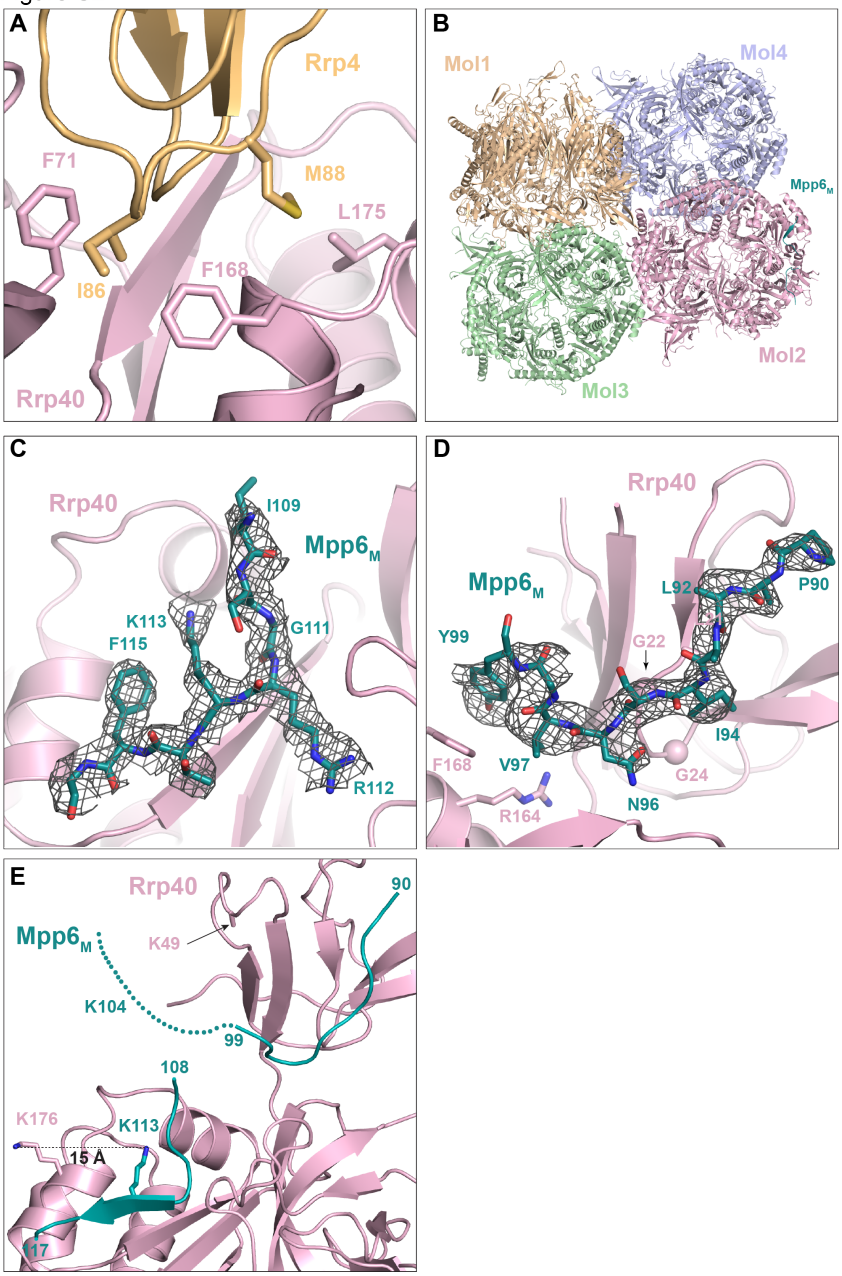

Figure S2, related to Figure 2. Crystallographic analysis of the Exo-9$_{Rrp4mut}$ – Mpp6$_M$ complex. **(A)** Typical Rrp40–Rrp4 interface forming lattice contacts in a representative yeast exosome crystal structure (PDB: 4IFD). Rrp4 is shown in orange and Rrp40 in salmon. Isoleucine 66 and methionine 68 of Rrp4 were mutated to glutamate (Rrp4$_{mut}$) to change crystal packing. **(B)** Packing of the four copies of the complexes present is in the asymmetric unit of the Exo-9$_{Rrp4mut}$ – Mpp6$_M$ crystal. The different copies are colored in brown, salmon, green and blue and related by non-crystallographic symmetry We note that the hydrophobic patch at Rrp4 I66 and Met68 is used to bind the Rrp6 nuclease domain (Makino et al., 2015; Wasmuth et al., 2014; Zinder et al., 2016). When crystallizing exosome complexes in the absence of Rrp6, this hydrophobic patch has a strong tendency to mediate protein-protein interactions with other complexes in the crystal lattice. (**C**) and (**D**) Snapshots of the refined electron density from the Mpp6–Rrp40 interface at the long segment (**C**) and the short segment, fitted tentatively with the Mpp6 sequence from Pro90 to Tyr99 (**D**). The refined 2mFo-DFc map (sharpened with -45 Å^2 B-factor) is contoured at 1.0 σ and superposed with the final model. Rrp40 is colored salmon, Mpp6 in cyan. (**E**) Superposition of Mpp6$_M$ onto the structure of yeast Exo-11 (PDB: 4IFD) to highlight the proximity of the two intermolecular crosslinks between Mpp6 and Rrp40 peptides observed by (Shi et al., 2015).

Figure S3

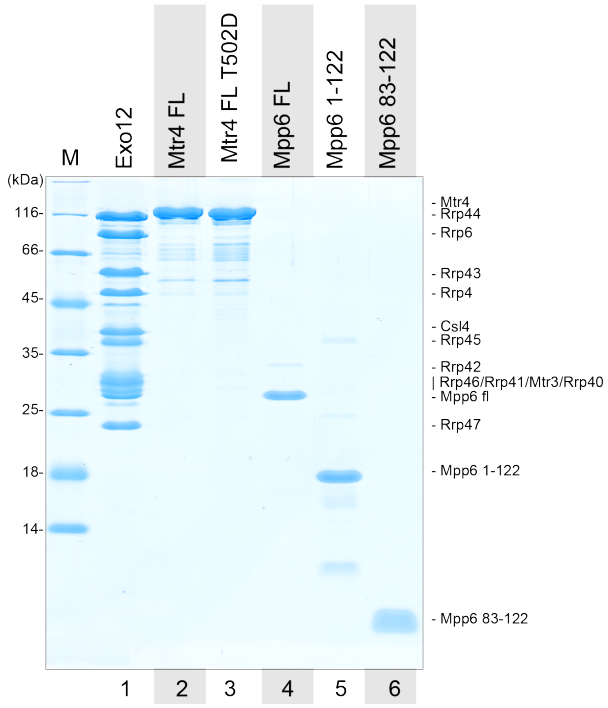

Figure S3, related to Figure 3. Proteins used in RNase protection assay.
15% SDS-PAGE gel stained with Instant Blue (Expedeon) showing the proteins used in the RNase protection experiment. 10 pmol of sample were loaded in lanes 1-4 and 40 pmol of sample in lanes 5 and 6.

Supplemental Experimental Procedures

Recombinant protein expression and purification

S. cerevisiae Mpp6 proteins (full-length, truncations and mutants) were expressed as His-GST-fusions in *E. coli* and purified as previously described (Schuch et al., 2014). The His_6-GST tag was cleaved using 3C protease, when required. Purification and assembly of the yeast exosome was performed as described in (Makino et al., 2013) with the exception that Rrp46 was truncated at the C-terminus (1-223) and Rrp4 at the N-terminus (51-359) to remove regions that were poorly ordered in the previous structures (Kowalinski et al., 2016). *S. cerevisiae* Mtr4 proteins (full-length and truncations) were purified as described in (Falk et al., 2014). The yeast Exo-9 – Mpp6 complex was reconstituted by mixing Exo-9 with 1.2 fold molar excess of Mpp6 full-length followed by gel filtration in a buffer containing 20 mM Hepes/NaOH pH 7.5, 100 mM NaCl and 2 mM DTT.
Purification and assembly of the *H. sapiens* Exo-9 complex was performed as described in (Greimann and Lima, 2008; Kowalinski et al., 2016). Human MPP6 residues 40-83 were tagged at the N-terminus with a His_6-thioredoxin-tag (His-Trx) and at the C-terminus with a $(Ser\text{-}Gly)_3$-linker and eGFP-StrepII-tag (eGFP-StrepII) to reduce proteolytic degradation. The resulting His-Trx-hMPP6-eGFP-StrepII fusion protein was expressed in *E. coli* and purified using Ni- and Streptactin affinity chromatography. The mutants were purified with the same protocols as the wild-type proteins with the exception of the yeast Mpp6-Cys184 substitution, where we replaced 2 mM DTT with 0.5 mM TCEP in the final buffer.

Endogenous protein purification

All yeast strains generated here are derivatives of the base strain BY4741 (MATa his3Δ1 leu2Δ0 met15Δ0 ura3Δ0). General yeast manipulations were conducted by standard methods with transformation by the lithium acetate method (Gietz and Schiestl, 2007). A C-terminal tandem affinity purification tag inspired by (Passmore et al., 2003) was engineered consisting of a 10-residues Glycine-Serine linker preceding a TwinStrep tag, followed by a 3C protease cleavage site and two IgG-binding domains of *Staphylococcus aureus* protein A. Yeast carrying tagged versions of exosome subunits were cultivated in 1 to 2 liters of YPD to an OD_{600} of 1 and harvested by centrifugation. The cell paste was

immediately frozen and pulverised in a freezer/mill (Spex). The powder was resuspended in lysis buffer (250 mM potassium phosphate pH 8.0, 1 mM EDTA, 0.1% NP40 (v/v), 0.5 mM DTT) containing complete protease inhibitor cocktail (Roche), clarified by centrifugation at 18000 g for 15 min and incubated 2 h at 4˚C with IgG-sepharose resin (GE Healthcare). Beads were washed three times with IPP250 (10 mM Tris pH 8.0, 250 mM NaCl, 0.1% NP40 (v/v)), resuspended in cleavage buffer (10 mM Hepes/NaOH pH 7.9, 50 mM KCl, 2 mM $MgCl_2$, 0.1% NP40 (v/v), 0.5 mM DTT) and incubated 2 h at room temperature with 1 µg 3C protease and 750 U Serratia marcescens nuclease. The eluate was incubated with StrepTactin resin (IBA) for 1 h at 4˚C, beads were washed three times with IPP250 and the final complex eluted in IPP250 supplemented with 2.5 mM D-desthiobiotin (Sigma). Eluates were precipitated with Trichloroacetic acid before separation on a 12% SDS PAGE and staining with InstantBlue (Expedeon).

Pull-down assays

For the pull-down reactions of the yeast proteins in Figures 1D and 2C, 1.0 µM of bait protein (GST-Mpp6) was pre-incubated with 1.2 µM of prey (Exo-9) in a in buffer containing 20 mM Hepes/NaOH pH 7.5, 100 mM NaCl, 2 mM DTT and 0.01% (v/v) NP-40 for 1 h at 0°C. Then the sample was incubated with GSH Sepharose (GE Healthcare) for 2 h at 4°C, washed three times with the same buffer, and eluted in 20 mM Tris/HCl pH7.5, 100 mM NaCl, 2 mM DTT, 0.01% (v/v) NP-40 and 30 mM reduced gluthathione. Input and pull-down fractions were analyzed on denaturing 12.5% SDS-PAGE and visualized with Coomassie staining.

For the pull-down reactions of the human proteins in Figures 2D and 2E, a total of 5 µg of tagged bait (His-Trx-$hMPP6^{40-83}$-eGFP-StrepII) was incubated with 1.2 molar excess of untagged prey (human EXO-9) in a volume of 50 µl in pull-down buffer (20 mM Tris/HCl pH 7.5, 100 mM NaCl, 0.01% (v/v) NP-40, 5 mM DTT). The high ionic strength buffer contained 500 mM NaCl instead of 100 mM NaCl. After incubation with GFP-binder resin for 1 h and three washing steps with pull-down buffer the resin was dried and taken up in SDS sample buffer and boiled for 3 min at 95°C to elute bound proteins. Input and pull-down fractions were analyzed on denaturing 12% SDS-PAGE.

RNase protection assay

For the RNase protection assays in Figure 3, the internally labeled 57-mer RNA substrate (5′ - $C(*UC)_{28}$ - 3′) was generated by *in vitro*-transcription in presence of a-^{32}P UTP using the MEGAshortscript kit (Ambion) and purified by poly-acrylamide gel electrophoresis. Typically, 10 pmol protein was mixed with 5 pmol internally labeled RNA in a final reaction volume of 20 µl (final buffer: 50 mM MES pH 6.0, 50 mM NaCl, 5 mM magnesium diacetate, 10% glycerol (v/v), 0.1% NP40 (v/v) and 1 mM DTT). Samples were incubated at 4°C for 1 h before treatment with 0.5 µl RNase A/T1 mix (Thermo Scientific) for 20 min at 20°C. The reaction was stopped by 10x dilution in a buffer containing 100 mM Tris pH 7.5, 150 mM NaCl, 300 mM sodium acetate, 10 mM EDTA and 1% (w/v) SDS. Protected RNA fragments were then extracted twice with phenol:chloroform:isoamyl-alcohol (25:24:1, (v/v/v), Invitrogen), precipitated with ethanol, separated on a 12% (w/v) denaturing poly-acrylamide gel and visualized by phosphorimaging.

Microscale Thermophoresis

For the microscale thermophoresis experiments in Figure 1A, Mpp6 S184C was labeled with red-maleimide following the manufactures protocol (MO-L004 Monolith, NanoTemper Technologies). 50 nM of labeled Mpp6-S184C (Mpp6-S184C*) was incubated with increasing concentrations of unlabeled Exo-9 in 50 mM Tris/HCl pH 7.4, 150 mM NaCl, 10 mM $MgCl_2$, 0.05% (v/v) Tween 20. The Exo-9 concentration series was produced by serial dilution (1:1). Thermophoresis was measured with an LED power of 40% and standard parameters on a NanoTemper Monolith NT.115 machine. Titrations were performed in triplicates and the data were analysed using the Thermophoresis and T-Jump strategy option with the MO software (NanoTemper Technologies).

Circular dichroism

Circular dichroism spectra (Figure S1B) were recorded on a Jasco J-715 spectropolarimeter in a 0.1-cm path length cuvette at 20°C. $Mpp6^{FL}$ was exchanged into a buffer containing 10 mM potassium phosphate pH 7.5, 50 mM sodium fluoride. Eight scans were taken from 250 to 190 nm in 1-nm increments and the scans were averaged, and the buffer spectrum was subtracted.

Crystallization and structure determination

The best diffracting crystals of the Exo-$9_{Rrp4mut}$ – $Mpp6_M$ complex were obtained at 12 mg/ml in 0.1 M Tris/Mops pH 7.5, 30 mM $MgCl_2$, 30 mM $CaCl_2$ and 30% PEG 8000/Ethylene glycol. Crystals were frozen directly from the drops and X-ray data were collected at 100 K at the beamline PXII (X10SA) of the Swiss Light Source (SLS) (Villigen, Switzerland). The crystals belong to the monoclinic space group $P2_1$ with four complexes in the asymmetric unit and diffracted to 3.2 Å resolution. Data processing was performed using the DIALS (Waterman et al., 2016), Xia2 (Winter, 2009) and AIMLESS (Evans and Murshudov, 2013) programs that are part of CCP4i2 (Winn et al., 2011). The structure of the Exo-$9_{Rrp4mut}$ – $Mpp6_M$ complex was solved by molecular replacement using the structure Exo-9 core from (PDB 5JEA) (Kowalinski et al., 2016) using PHASER (McCoy et al., 2007) within Phenix (Adams et al., 2010). Model building was performed using COOT (Emsley et al., 2010) and the structure was refined using phenix.refine (Afonine et al., 2012), Refmac (Murshudov et al., 2011) and Buster (version 2.10.3) (Smart et al., 2012). The stereochemistry of the model was assessed using MolProbity (Davis et al., 2007).

Supplemental References

Adams, P.D., Afonine, P.V., Bunkoczi, G., Chen, V.B., Davis, I.W., Echols, N., Headd, J.J., Hung, L.-W., Kapral, G.J., Grosse-Kunstleve, R.W., McCoy, A.J., Moriarty, N.W., Oeffner, R., Read, R.J., Richardson, D.C., Richardson, J.S., Terwilliger, T.C., Zwart, P.H., 2010. PHENIX: a comprehensive Python-based system for macromolecular structure solution. Acta Crystallogr D Biol Crystallogr 66, 213–221.

Afonine, P.V., Grosse-Kunstleve, R.W., Echols, N., Headd, J.J., Moriarty, N.W., Mustyakimov, M., Terwilliger, T.C., Urzhumtsev, A., Zwart, P.H., Adams, P.D., 2012. Towards automated crystallographic structure refinement with phenix.refine. Acta Crystallogr D Biol Crystallogr 68, 352–367.

Davis, I.W., Leaver-Fay, A., Chen, V.B., Block, J.N., Kapral, G.J., Wang, X., Murray, L.W., Arendall, W.B., Snoeyink, J., Richardson, J.S., Richardson, D.C., 2007. MolProbity: all-atom contacts and structure validation for proteins and nucleic acids. Nucleic Acids Research 35, W375–83. doi:10.1093/nar/gkm216

Emsley, P., Lohkamp, B., Scott, W.G., Cowtan, K., 2010. Features and development of Coot. Acta Crystallogr D Biol Crystallogr 66, 486–501.

Evans, P.R., Murshudov, G.N., 2013. How good are my data and what is the resolution? Acta Crystallogr D Biol Crystallogr 69, 1204–1214.

Falk, S., Weir, J.R., Hentschel, J., Reichelt, P., Bonneau, F., Conti, E., 2014. The Molecular Architecture of the TRAMP Complex Reveals the Organizationand Interplay of Its Two Catalytic Activities. Molecular Cell 55, 856–867.

Gietz, R.D., Schiestl, R.H., 2007. High-efficiency yeast transformation using the LiAc/SS carrier DNA/PEG method. Nat Protoc 2, 31–34.

Greimann, J., Lima, C., 2008. Reconstitution of RNA exosomes from human and Saccharomyces cerevisiae cloning, expression, purification, and activity assays. Meth. Enzymol. 448, 185–210.

Kowalinski, E., Kögel, A., Ebert, J., Reichelt, P., Stegmann, E., Habermann, B., Conti, E., 2016. Structure of a Cytoplasmic 11-Subunit RNA Exosome Complex. Molecular Cell 63, 125–134.

Li, X., Romero, P., Rani, M., Dunker, A., Obradovic, Z., 1999. Predicting Protein Disorder for N-, C-, and Internal Regions. Genome Inform Ser Workshop Genome Inform 10, 30–40.

Makino, D.L., Baumgärtner, M., Conti, E., 2013. Crystal structure of an RNA-bound 11-subunit eukaryotic exosome complex. Nature 495, 70–75.

Makino, D.L., Schuch, B., Stegmann, E., Baumgärtner, M., Basquin, C., Conti, E., 2015. RNA degradation paths in a 12-subunit nuclear exosome complex. Nature 524, 54–58.

McCoy, A.J., Grosse-Kunstleve, R.W., Adams, P.D., Winn, M.D., Storoni, L.C., Read, R.J., 2007. Phaser crystallographic software. J. Appl. Cryst (2007). 40, 658-674 1–17.

Murshudov, G.N., Skubák, P., Lebedev, A.A., Pannu, N.S., Steiner, R.A., Nicholls, R.A., Winn, M.D., Long, F., Vagin, A.A., 2011. REFMAC5 for the refinement of macromolecular crystal structures. Acta Crystallogr D Biol Crystallogr 67, 355–367.

Passmore, L.A., McCormack, E.A., Au, S.W.N., Paul, A., Willison, K.R., Harper, J.W., Barford, D., 2003. Doc1 mediates the activity of the anaphase-promoting complex by contributing to substrate recognition. EMBO J. 22, 786–796.

Schuch, B., Feigenbutz, M., Makino, D.L., Falk, S., Basquin, C., Mitchell, P., Conti, E., 2014. The exosome-binding factors Rrp6 and Rrp47 form a composite surface for recruiting the Mtr4 helicase. EMBO J. 33, 2829–2846.

Shi, Y., Pellarin, R., Fridy, P.C., Fernandez-Martinez, J., Thompson, M.K., Li, Y., Wang, Q.J., Sali, A., Rout, M.P., Chait, B.T., 2015. A strategy for dissecting the architectures of native macromolecular assemblies. Nat. Methods 12, 1135–1138.

Smart, O.S., Womack, T.O., Flensburg, C., Keller, P., Paciorek, W., Sharff, A., Vonrhein, C., Bricogne, G., 2012. Exploiting structure similarity in refinement: automated NCS and target-structure restraints in BUSTER. Acta Crystallogr D Biol Crystallogr 68, 368–380.

Wasmuth, E.V., Januszyk, K., Lima, C.D., 2014. Structure of an Rrp6-RNA exosome complex bound to poly(A) RNA. Nature 511, 435–439.

Waterman, D.G., Winter, G., Gildea, R.J., Parkhurst, J.M., Brewster, A.S., Sauter, N.K., Evans, G., 2016. Diffraction-geometry refinement in the DIALS framework. Acta Crystallogr D Struct Biol 72, 558–575.

Winn, M.D., Ballard, C.C., Cowtan, K.D., Dodson, E.J., Emsley, P., Evans, P.R., Keegan, R.M., Krissinel, E.B., Leslie, A.G.W., McCoy, A., McNicholas, S.J., Murshudov, G.N., Pannu, N.S., Potterton, E.A., Powell, H.R., Read, R.J., Vagin, A., Wilson, K.S., 2011. Overview of the CCP4 suite and current developments. Acta Crystallogr D Biol Crystallogr 67, 235–242.

Winter, G., 2009. xia2: an expert system for macromolecular crystallography data reduction. J. Appl. Cryst (2010). 43, 186-190 1–5.

Zinder, J.C., Wasmuth, E.V., Lima, C.D., 2016. Nuclear RNA Exosome at 3.1 Å Reveals Substrate Specificities, RNA Paths, and Allosteric Inhibition of Rrp44/Dis3. Molecular Cell 64, 734–745.